Highly Reproducible Epitaxial Growth of Wafer-Scale Single-Crystal Monolayer MoS_2 on Sapphire

Pengfei Yang, Fachen Liu, Xuan Li, Jingyi Hu, Fan Zhou, Lijie Zhu, Qing Chen, Peng Gao,* and Yanfeng Zhang**

2D semiconducting transition-metal dichalcogenides (TMDs) have attracted considerable attention as channel materials for next-generation transistors. To meet the industry needs, large-scale production of single-crystal monolayer TMDs in highly reproducible and energy-efficient manner is critically significant. Herein, it is reported that the high-reproducible, high-efficient epitaxial growth of wafer-scale monolayer MoS_2 single crystals on the industry-compatible sapphire substrates, by virtue of a deliberately designed "face-to-face" metal-foil-based precursor supply route, carbon-cloth-filter based precursor concentration decay strategy, and the precise optimization of the chalcogenides and metal precursor ratio (i.e., S/Mo ratio). This unique growth design can concurrently guarantee the uniform release, short-distance transport, and moderate deposition of metal precursor on a wafer-scale substrate, affording high-efficient and high-reproducible growth of wafer-scale single crystals (over two inches, six times faster than usual). Moreover, the S/Mo precursor ratio is found as a key factor for the epitaxial growth of MoS_2 single crystals with rather high crystal quality, as convinced by the relatively high electronic performances of related devices. This work demonstrates a reliable route for the batch production of wafer-scale single-crystal 2D materials, thus propelling their practical applications in highly integrated high-performance nanoelectronics and optoelectronics.

1. Introduction

2D semiconducting transition-metal dichalcogenides (TMDs), most with a formula of MX_2 (M=Mo, W; X=S, Se, etc.), have stood as fertile platforms in future electronics and photonics-related applications, owing to their dangling-bond-free surfaces, tunable bandgaps, strong light-matter interactions, and ultrathin thickness down to the 2D limit.[1–5] However, to fully exploit their extraordinary potential, a key premise is to realize the wafer-scale growth of single-crystal MX_2 monolayers on industrial-compatible substrates.

To date, epitaxial growth has been recognized as the most promising route for the preparation of wafer-scale single-crystal 2D materials (e.g., graphene,[6,7] *h*-BN,[8,9] MoS_2[10,11,12]), through the seamless coalescence of unidirectional 2D domains into single-crystal films on lattice/symmetry matching substrates. Recently, our group has realized the epitaxy of centimeter-scale uniform monolayer MoS_2 single-crystals on a series of Au single crystals vicinal to (111) and (110), through the seamless stitching of unidirectionally orientated triangular or ribbon-shaped domains.[13–15] This was realized by the unidirectional growth of monolayer MoS_2 along energetically favorable Au steps, as well as the perfect lattice match of MoS_2 and Au(111) or Au(110).

Nevertheless, for their direct applications in electronic applications, the direct growth of wafer-scale MX_2 single-crystals on insulating substrates (e.g., sapphire) should be more attractive than that on metals, in terms of their industrial compatible and easily transferable features.[16,17] Very recently, epitaxial growth

P. Yang, J. Hu, F. Zhou, L. Zhu, Y. Zhang
School of Materials Science and Engineering
Peking University
Beijing 100871, P. R. China
E-mail: yanfengzhang@pku.edu.cn

P. Yang, X. Li, J. Hu, F. Zhou, Q. Chen, Y. Zhang
Center for Nanochemistry
Academy for Advanced Interdisciplinary Studies
Peking University
Beijing 100871, P. R. China
E-mail: qingchen@pku.edu.cn

F. Liu, P. Gao
Electron Microscopy Laboratory, and International Center for Quantum Materials
School of Physics
Peking University
Beijing 100871, P. R. China
E-mail: pengg@pku.edu.cn

X. Li, Q. Chen
Key Laboratory for the Physics and Chemistry of Nanodevices
School of Electronics
Peking University
Beijing 100871, P. R. China

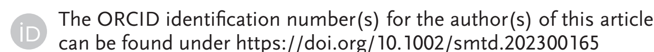
The ORCID identification number(s) for the author(s) of this article can be found under https://doi.org/10.1002/smtd.202300165

DOI: 10.1002/smtd.202300165

© 2023 Wiley-VCH GmbH

of wafer-scale monolayer MoS_2 and WS_2 single-crystal films have been achieved on C-A and A sapphire substrates, by using MoO_3 + S, WO_3 + NaCl + S as precursors, respectively.[18,19] The nucleation and growth of monolayer MoS_2 and WS_2 domains preferred to along the <10$\bar{1}$0> step edges of sapphire, inducing the unidirectional alignment of monolayer MX_2 domains on sapphire. However, the internal mechanisms were mainly discussed from the guiding effects of substrate step edges or the lattice/symmetry matching effects on the unidirectional growth of MX_2 monolayers, other basic factors for the epitaxial growth, e.g., growth kinetics, and precursor ratio, remain unexplored. More significantly, more portable routes for scaling up the growth to even larger sizes that are compatible with silicon-based devices (from 2 inches to even larger sizes) still need to be developed.

In the current chemical vapor deposition (CVD) growth process, transition metal oxides (*e.g.*, MoO_3 and WO_3) are the most used metal precursors. However, due to their high vaporizing temperature (MoO_3: 530 °C, WO_3: 850 °C) and the upstream transport design, the metal precursor concentration gradually decreased along the gas flow direction, usually inducing nonuniform growth from upstream to downstream locations with the sample size limited to centimeter scale.[20–25] To tackle this, many attempts have been made, through introducing oxygen or hydroxide promoters,[26,27] designing multisource feeding configurations,[28] or using vertical CVD setup (gas flow from top to bottom).[29] Recently, our group has designed a “face-to-face” metal precursor supply route and realized the synthesis of 6 inch uniform monolayer MoS_2 film on soda-lime glass substrate at ≈720 °C.[30] The face-to-face configuration of Mo foil and glass substrate guaranteed the uniform release of Mo-based precursors by introducing minor O_2, enabling homogeneous nucleation and growth of monolayer MoS_2. However, this synthetic route cannot be simply duplicated in the growth of monolayer MoS_2 on sapphire that needs a higher growth temperature (> 900 °C), since excessive Mo-based precursors will be generated, yielding a high density of nucleation site and resulting in the growth of small-sized or thicker flakes.

Herein, we have designed a portable CVD route for the highly reproducible growth of wafer-scale monolayer MoS_2 single-crystals on the industrial compatible C-A sapphire substrate, by combining a “face-to-face” metal precursor supply route with “carbon cloth filter” on template design, under the precise control of the thermodynamics and growth kinetics. The superiorities of this route can be summarized as follows: 1) the “face-to-face” metal precursor feeding route with an over-positioned Mo foil guarantees the homogeneous release of Mo-related precursors, enabling the wafer-scale uniform synthesis of monolayer MoS_2 films; 2) the carbon cloth filter placed over the substrate is designed as a physical barrier to prevent the excessive deposition of metal precursors, allowing the evolution of low-density nucleus and thus large domain size growth of MoS_2; 3) high ratio of S/Mo precursors is designed for mediating the growth under thermodynamically equilibrium state, which is beneficial for the growth of unidirectionally aligned MoS_2 triangular crystals, thus laying foundation for their seamless stitching into single crystal films. This work aims at developing a portable strategy for the highly reproducible growth of monolayer MX_2 single-crystal wafers, thus offering new insights into the orientation-controlled growth mechanisms from the growth kinetics viewpoint, which is expected to propel the batch production of wafer-scale monolayer MX_2 crystals and their practical applications in the next generation of highly integrated electronic and optoelectronic devices.

2. Results and Discussion

The epitaxial growth of monolayer MoS_2 single crystals was performed on C-A 1° sapphire substrates in a low-pressure CVD system equipped with a 3-inch quartz tube, by using Mo foil and S powder as precursors (**Figure 1**a; Figure S1, Supporting Information). The commensurability between MoS_2 lattice and sapphire lattice ($a_{sapphire}/a_{MoS2}$ = 3/2),[31] and the guiding effect of sapphire step edges are proposed to direct the unidirectionally aligned growth of monolayer MoS_2 single crystals, as reported in the previous reports.[18,32,33] The Mo foil was folded as a “bridge” and placed on top of the sapphire substrate in a “face-to-face” geometry with a distance of ≈1 cm. Accordingly, homogenous and continuous supply of Mo-based precursor (MoO_{3-x} by loading trace amount of O_2) is achieved on C-A 1°sapphire substrates, resulting in uniform nucleation and growth of MoS_2 monolayers. X-ray photoemission (XPS) data confirm its chemical composition (Figure S2, Supporting Information), and atomic force microscope (AFM) height profile across the edge of the typical MoS_2 domain justifies its monolayer characteristics (≈0.7 nm, Figure S3, Supporting Information).

To obtain the unidirectionally aligned MoS_2 monolayers on sapphire, the growth temperature was set at ≈950 °C. Meanwhile, to prevent excessive precursor release at high temperatures, a piece of carbon cloth filter was placed on the sapphire substrate, serving as a physical barrier to greatly reduce the deposition of Mo and S-related precursors on sapphire. The carbon cloth was selected considering its porous structure (SEM image in Figure S4, Supporting Information), high melting point (> 1000 °C) and chemical inertness to precursors, etc. Accordingly, the nucleation density of MoS_2 on sapphire (≈950 °C for 4 min) is largely reduced, along with the domain size increasing greatly from ≈10 to ≈30 µm (Figure 1b,c). Notably, the derived monolayer MoS_2 domains are featured with equilateral triangular morphology on sapphire. And the orientation statistic shows a proportion of ≈99% across a 2-inch sapphire wafer for the uniformly orientated domains (Figure S5, Supporting Information). Besides, the edges of monolayer MoS_2 domains are preferentially aligned along the step edges of sapphire substrates, following the step-edge-guided growth feature, in good accordance with the literature of monolayer MoS_2 grown on C-A sapphire.[18] More intriguingly, by prolonging the growth time from ≈4 to 10 min, these unidirectionally orientated monolayer MoS_2 domains gradually merged together, with the formation of a 2-inch continuous single crystalline film (Figure 1d). Notably, this growth time for monolayer film (≈10 min) is six times faster than that by using up-streamed MoO_3 precursor (≈60 min) design on sapphire (at comparable growth temperature ≈850—1000 °C).[18] This is possibly due to the relatively short diffusion distance between Mo source and substrate (≈ 1 cm).

Except for the rather high growth efficiency, the robust growth reproducibility and scalability are also the unique traits of the developed synthetic route. To demonstrate this, a batch of 7 pieces 2-inch uniform monolayer MoS_2 film on sapphire wafers was produced (Figure 1e). The uniform yellow-green color highly

© 2023 Wiley-VCH GmbH

23669608, 2023, 7, Downloaded from https://onlinelibrary.wiley.com/doi/10.1002/smtd.202300165 by Peking University Health, Wiley Online Library on [16/11/2023]. See the Terms and Conditions (https://onlinelibrary.wiley.com/terms-and-conditions) on Wiley Online Library for rules of use; OA articles are governed by the applicable Creative Commons License

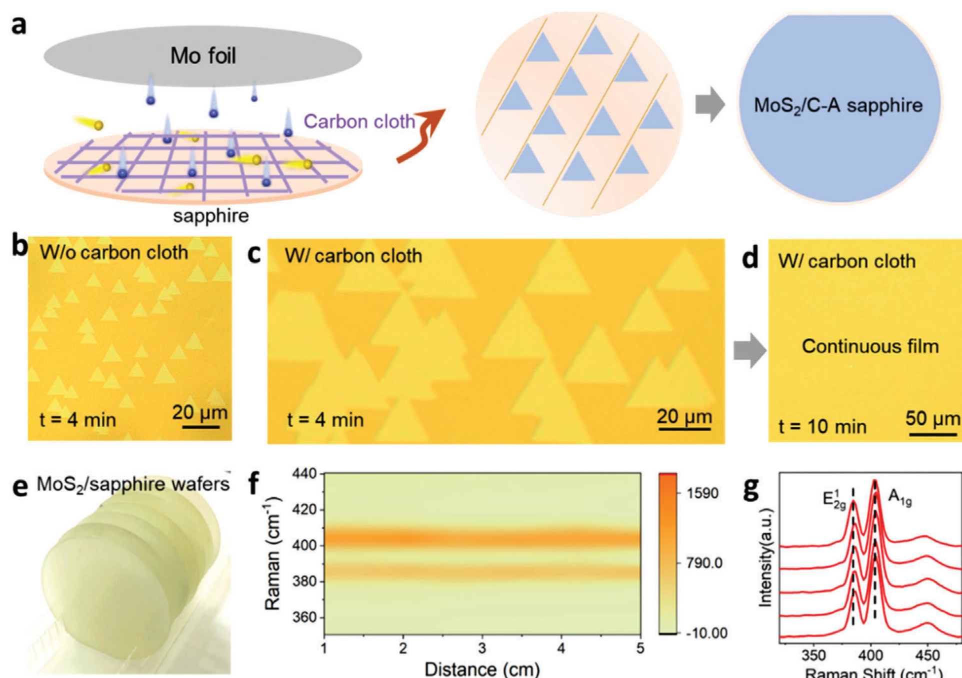

Figure 1. Epitaxial growth of 2-inch uniform monolayer MoS_2 single-crystal on sapphire with high reproducibility and growth efficiency. a) Schematic illustration of the carbon-cloth-shield over sapphire template assisted growth of monolayer MoS_2/sapphire via a "face-to-face" positioned Mo-foil based precursor design route (left), and the evolution of mono-oriented monolayer MoS_2 triangular crystals and wafer-scale single crystal film (right). b) Typical optical microscopy (OM) image of small-size monolayer MoS_2 triangles (edge length ≈10 μm) synthesized on sapphire without the assistance of carbon-cloth-shield over sapphire (growth time ≈4 min). c) OM image of unidirectionally oriented monolayer MoS_2 triangular domains (edge length ≈30 μm) synthesized on sapphire with the assistance of carbon-cloth-shield (growth time ~4 min). d) OM image showing the formation of continuous monolayer MoS_2 film at extended growth time of 10 min. e) Reproducible growth of monolayer MoS_2 single crystals on 2-inch sapphire wafers. f) Color-coded images of the typical Raman modes collected from 25 positions with an interval of 2 mm along a randomly selected direction of the wafer. g) Raman spectra extracted randomly from five positions over the continuous MoS_2 monolayer to show its uniform monolayer thickness.

suggests the good thickness uniformity at a macroscopic level. Randomly selected Raman data to exhibit its monolayer feature, based on the fixed frequency difference ($\Delta = 18 \pm 0.5$ cm^{-1}, E^1_{2g} and A_{1g} peaks fixed at ≈385 and ≈403 cm^{-1}, respectively) (Figure 1f,g). Briefly, through a perfect combination of the Mo-foil-based metal precursor supply route with the carbon cloth filter on template strategy, 2-inch scale uniform monolayer MoS_2 single crystal films can be achieved on C-A 1° sapphire. This wafer size is only limited by the size of the CVD furnace, and it can be further scaled up. Notably, the current growth route can mediate the highly reproducible, high-efficiency growth of wafer-scale monolayer MoS_2 single crystal films on sapphire substrates, which should be more compatible with industrial production.

Low-energy electron diffraction (LEED) characterizations were then selected to reveal the single crystallinity of the as-grown monolayer MoS_2 on sapphire. Three bright diffraction spots can be observed universally over the sample surface, in analog with that of other C_3 symmetric crystals (e.g., monolayer *h*-BN single-crystal on Cu(110)[8]). And all the patterns present an identical lattice orientation, which highly indicates the single crystallinity of the monolayer MoS_2 film on sapphire (**Figure 2**b). Otherwise, the absence of satellite spots addresses the relatively weak adlayer-substrate interaction. Moreover, the sharp A exciton peak (≈665 nm), narrow full-width at half-maximum (≈55 meV) in the photoluminescence (PL) spectra (Figure 2c), and the uniform PL mapping images highly suggest the uniform monolayer thickness of MoS_2/sapphire in a 2-inch wafer scale (Figure 2d, in randomly selected three locations). Notably, second-harmonic generation (SHG) measurement was reported to be an effective route for identifying the GB-like defects in 2D materials (imaged as depressed contrasts).[34,35] In this work, the SHG mapping images of as-grown monolayer MoS_2/sapphire reveal almost no obvious contrast difference over the sample surfaces (as representatively shown in Figure 2e), which should serve as direct evidence for revealing the single crystallinity of the as-grown monolayer MoS_2 sample. In addition, the parallelly aligned triangular holes in the monolayer MoS_2 film after the O_2 etching process (Figure S6, Supporting Information) also confirmed the single crystallinity of the film. Overall, based on onsite electron diffraction, Raman spectroscopy, and SHG characterizations, the CVD-derived 2-inch monolayer MoS_2 single crystal wafers can be inferred to be featured with uniform monolayer thickness, almost free of domain boundary and thus relatively high crystal quality.

Exploring the fundamental mechanisms for the unidirectional growth and the seamless patching of monolayer MoS_2 film on sapphire should be a critical issue, while still not fully addressed. In our experiment, the precise control of the S/Mo precursor ratio in the CVD growth process was found to be a key factor to mediate the domain orientations and morphologies of MoS_2 on sapphire. By increasing the S/Mo ratio (increasing the sulfur weight from

 © 2023 Wiley-VCH GmbH

23669608, 2023, 7, Downloaded from https://onlinelibrary.wiley.com/doi/10.1002/smtd.202300165 by Peking University Health, Wiley Online Library on [16/11/2023]. See the Terms and Conditions (https://onlinelibrary.wiley.com/terms-and-conditions) on Wiley Online Library for rules of use; OA articles are governed by the applicable Creative Commons License

23669608, 2023, 7, Downloaded from https://onlinelibrary.wiley.com/doi/10.1002/smtd.202300165 by Peking University Health, Wiley Online Library on [16/11/2023]. See the Terms and Conditions (https://onlinelibrary.wiley.com/terms-and-conditions) on Wiley Online Library for rules of use; OA articles are governed by the applicable Creative Commons License

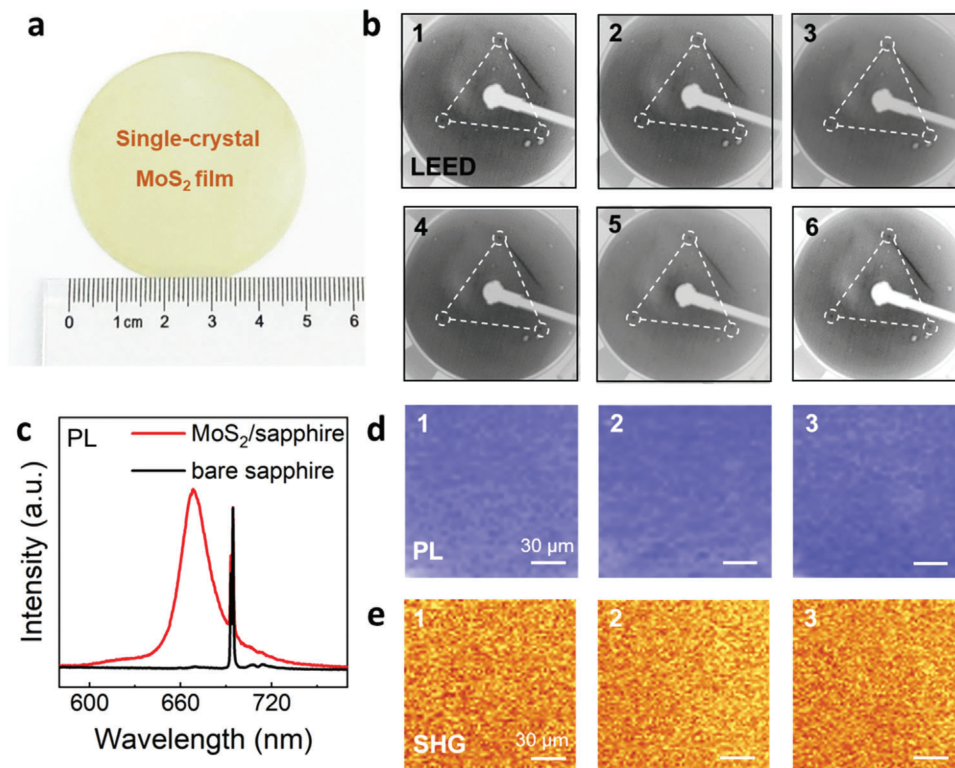

Figure 2. Multiscale characterizations of the uniform monolayer thickness and 2-inch scale uniform single crystallinity of the CVD-derived monolayer MoS_2 on sapphire. a) Photograph of a 2-inch uniform monolayer MoS_2 film on sapphire. b) Representative LEED patterns collected from six typical locations of the continuous 2-inch scale MoS_2 film showing nearly the identical lattice orientation (with electron beam diameter of 1 mm). c) Representative PL spectrum (peak position ≈665 nm) of the as-grown monolayer MoS_2 film on sapphire. The narrow full-width at half-maximum value (≈56 meV) confirms its rather high crystallinity. d) Representative PL mapping on the A exciton (≈667 nm) intensity of the monolayer MoS_2 film showing homogenous contrast, and thus highly uniform crystal quality and its monolayer thickness. e) Representative SHG mapping of the monolayer MoS_2 film showing homogenous contrast, highly indicating the domain boundary free and thus the single crystallinity of the 2-inch scale monolayer MoS_2 film.

≈6, ≈8 to ≈ 10 g), the morphologies of monolayer MoS_2 domains transform from triangles/quasi-trapezoids with curved edges to equilateral triangles with straight edges (**Figure 3**a–d, representative AFM images in Figure S6, Supporting Information). Further increasing the S feeding amount usually results in the growth of additional layers (Figur S7, Supporting Information). Notably, the orientations of equilateral triangular MoS_2 domains can be identified by OM images based on their straight edges, while it is not fit for the quasi-trapezoid shaped domains with irregular edges.

To explore their lattice orientations and patching behaviors, Raman, PL, and SHG characterizations were performed. A typical monolayer MoS_2 aggregate consisting of three coalescent domains with curved-edged trapezoids is presented in the OM image (Figure 3e). The homogenous color contrast in Raman mapping (of A_{1g} peak intensity) indicates the uniform monolayer thickness (Figure 3f). Nevertheless, a darkesingle GB line is visualized in the PL mapping image linking the neighboring domains (indicated by a yellow arrow in Figure 3g). Moreover, the existence of GBs at the domain patching boundaries is also confirmed by SHG mapping, showing similar depressed line-shaped contrasts, as indicated by yellow arrows in Figure 3h (also shown in Figure S7, Supporting Information). In contrast, the merged monolayer MoS_2 aggregates with regular triangular shapes (Figure 3i) are stitched well at the patching interfaces, as evidenced by the highly uniform color contrasts in Raman, PL, and SHG mapping images (Figure 3j–l).

To explore the patching behaviors of these two kinds of monolayer MoS_2 aggregates (derived at S = 8 and 10 g) at an atomic scale, transmission electron microscopy (TEM) and STEM characterizations were then conducted on the transferred samples. Low-magnified STEM image of two partially merged curve-edged monolayer MoS_2 domains (derived at S = 8 g) is displayed in **Figure 4**a. Corresponding STEM image located between the two domains shows a bright stripe-shaped contrast with a width of ≈130 nm (Domain 1 and Domain 2) (Figure 4b), wherein a specific moiré pattern appears with a period of ≈1.20 nm (Figure 4c,d). This indicates the formation of an overlapped bilayer region between the two adjacent MoS_2 domains. Moreover, atomic resolution STEM images (Figure 4c,d) captured at both borders reveal two domains with a relative misorientation of ≈14.6°, as verified by the corresponding 2D fast Fourier transform (FFT) analyses (inset of Figure 4c,d). The simulated atomic model shows a moiré period of ≈1.22 nm (Figure 4e), consistent with the experimental data.

Notably, the formation of such overlapping GBs was also reported in merged disorientated monolayer graphene/Cu(111),[36] *h*-BN/Fe,[37] and $MoS_2/SiO_2/Si$,[38] which

© 2023 Wiley-VCH GmbH

23669608, 2023, 7, Downloaded from https://onlinelibrary.wiley.com/doi/10.1002/smtd.202300165 by Peking University Health, Wiley Online Library on [16/11/2023]. See the Terms and Conditions (https://onlinelibrary.wiley.com/terms-and-conditions) on Wiley Online Library for rules of use; OA articles are governed by the applicable Creative Commons License

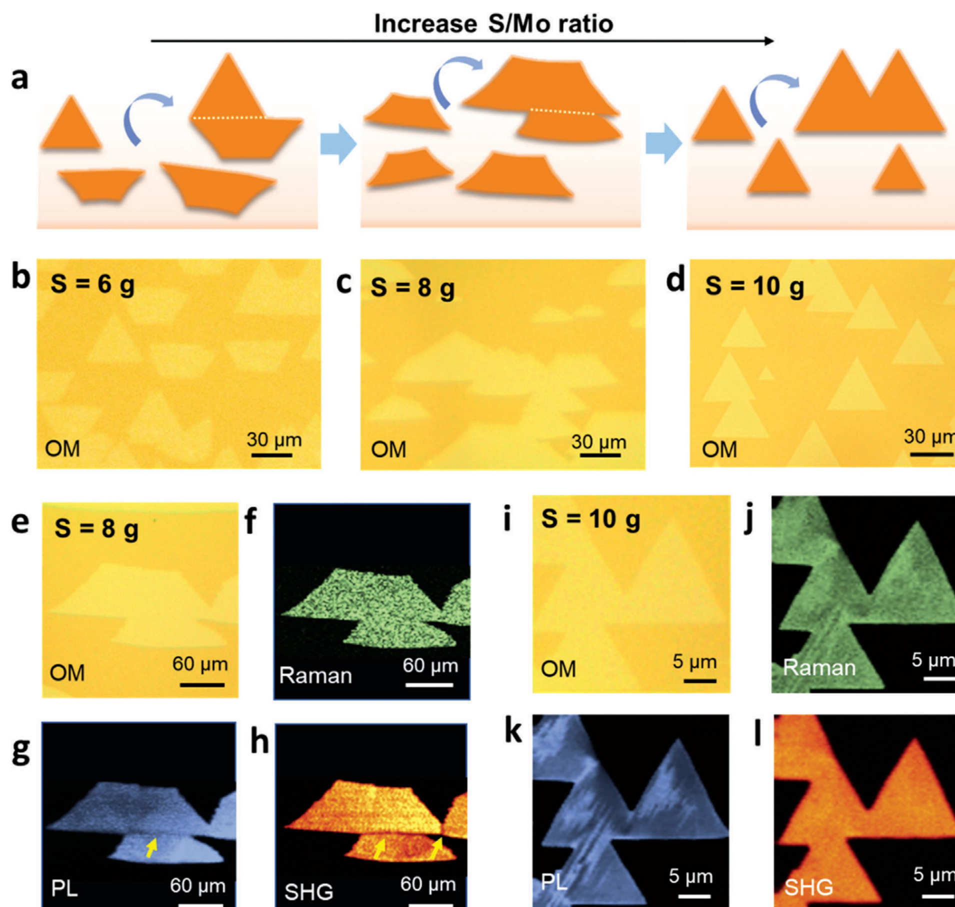

Figure 3. High S/Mo ratio inducing the unidirectional growth of equilateral triangular shaped monolayer MoS_2 domains. a) Schematic diagram regarding the morphology evolutions and patching behaviors of monolayer MoS_2 domains varying from curve-edged triangles/trapezoids to sharp-edged equilateral triangles. b–d) Large-area OM images of the typical morphologies of as-grown monolayer MoS_2 domains with S precursor amount varying from 6, 8to 10 g, respectively, with other growth parameters keeping constant (≈950 °C for 3 min). A high S/Mo ratio is beneficial for the formation of equilateral triangular MoS_2 domains with uniform orientation. e) Representative OM image of a monolayer MoS_2 aggregate composed by three merged curve-edged trapezoids. f–h) Corresponding Raman, PL, and SHG mapping of the monolayer MoS_2 aggregate in (e), showing obvious line-shaped intensity drop at the patching boundaries (marked with yellow arrows in (g,h). The quasi-trapezoid shaped monolayer MoS_2 domains with curved edges tend to merge with the evolution of GBs at the patching boundaries. i) Representative OM image of a monolayer MoS_2 aggregate composed by four sharp-edged equilateral triangular domains with a uniform orientation. j–l) Corresponding Raman, PL and SHG mapping images of the monolayer MoS_2 aggregate in (i) showing homogenous contrasts at the stitching boundaries. The unidirectionally oriented monolayer MoS_2 triangular domains tend to be merged seamlessly at the merging boundary.

was proposed to be due to the existence of strain during the coalescence process. Reactive molecular dynamics simulations suggested that the strain was induced by the continued growth of MoS_2 crystals during coalescence, along with the insertion of atoms at unsaturated defects along the GB. In our case, the strain may also arise from the stacking of monolayer MoS_2 on the corrugated sapphire substrate with high density of steps. Notably, the height of a single sapphire step (c/6, ≈0.2 nm) is much less than that of a monolayer MoS_2 (≈0.7 nm). Thereby, when two disorientated monolayer MoS_2 domains encounters, the uphill MoS_2 domain from a neighboring terrace is inclined to propagate and pass over the downhill MoS_2 layer, inducing the formation of an overlapping GB at the domain boundary region.

However, the case is totally different for the straight-edged triangular MoS_2 domains derived at high S/Mo conditions. A typical low-magnified STEM image of merged straight-edged MoS_2 domains is displayed in **Figure 5**a. According to the atomically resolved STEM images, the lattices of the two adjacent domains (Figure 5c,d) are aligned along the same orientation and patched seamlessly at the merging zones (Figure 5e). Additionally, all the randomly selected selective-area electron diffraction (SAED) patterns present nearly the identical lattice orientation (deviation smaller than ± 0.2°), reconfirming the single crystallinity all over the aggregate (Figure 5g). In this regard, by prolonging the growth time, the unidirectionally aligned monolayer MoS_2 domains can be merged into single crystal film, featured with rather high crystal quality.

The distinct domain orientations of monolayer MoS_2 domains derived at different S/Mo ratios should relate to the different orientations of MoS_2 nuclei formed at the initial growth stage. Notably, the MoS_2 monolayer preferentially nucleates along the C-A sapphire steps for these two cases (evidenced by the AFM

© 2023 Wiley-VCH GmbH

23669608, 2023, 7, Downloaded from https://onlinelibrary.wiley.com/doi/10.1002/smtd.202300165 by Peking University Health, Wiley Online Library on [16/11/2023]. See the Terms and Conditions (https://onlinelibrary.wiley.com/terms-and-conditions) on Wiley Online Library for rules of use; OA articles are governed by the applicable Creative Commons License

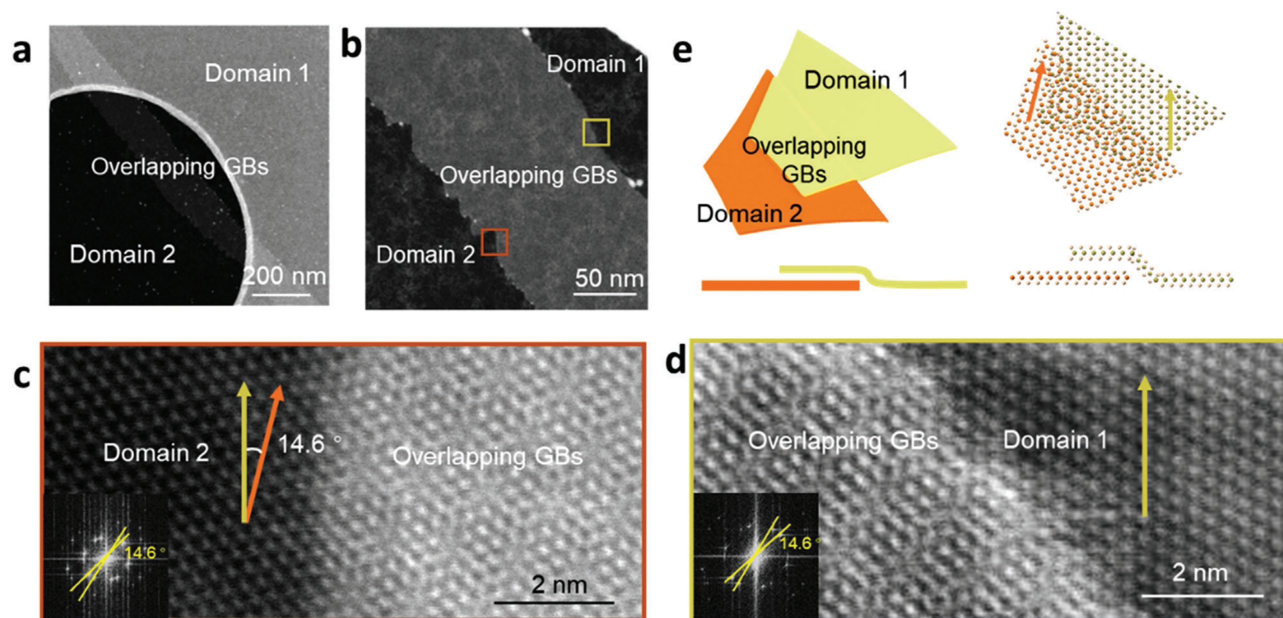

Figure 4. STEM characterizations of the atomic scale structures of the overlapped GBs evolved in the aggregation of disorientated, curve-edged monolayer MoS_2 trapezoids. a) Low-magnified STEM image showing the overlapping GBs (featured with a bright stripe) formed in the aggregation of disorientated monolayer MoS_2 trapezoids. b) Magnified STEM image of the transitional region from the stacked GBs to the adjacent monolayer domain. c,d) Atomic-resolution STEM image of the borders of the bilayer GBs between Domain 1 ((d) marked by the greeny-ellow square region in (b)), and Domain 2 ((c)marked by the orange square region in (b)), respectively. The bilayer region displays a specific moiré pattern formed by disoriented monolayer domains (with a period of ≈1.22 nm). The crystal orientations of Domains 1 and 2 are indicated by greenyellow and orange arrows, respectively, with a relative misorientation of ≈14.6°. Insets: FFT patterns of the regions in (c) and (d). e) Schematic illustration of the overlapping GBs formed by two disoriented MoS_2 trapezoid shaped domains (left panel). The simulated stacked GB region exhibits a typical moiré superstructure with a period of ≈1.20 nm (right panel), in good agreement with the experimental data.

images in Figure S6, Supporting Information), considering their lower adsorption energies than that on the terraces.[39] However, due to the locally meandering feature of step edges, a narrow orientation distribution of the nuclei should be induced. Previous studies have reported that a relatively low concentration of Mo can slow down the growth rate and switch the growth processes from kinetic to thermodynamic regimes, inducing the edge morphology of MoS_2 domains transformfrom curved to straight edge shapes.[40,41] Hereby, the growth process of monolayer MoS_2 domains under different S/Mo conditions can be inferred as follows. Under a low S/Mo condition, relatively high dense Mo vapor triggers fast kinetically driven growth of crystals, inducing the formation of monolayer MoS_2 domains with curved edges. In this case, the nuclei do not have enough time to move into the energetically favorable lattice locations, inducing the formation of disaligned MoS_2 domains relative to sapphire substrate. In contrast, a high S/Mo condition guarantees the growth under thermodynamic equilibrium states, where the nuclei may rotate and align to the substrate lattice, inducing the evolution of equilateral triangular shaped domains with a uniform orientation. In this regard, the orientation-controlled growth of monolayer MoS_2 single-crystals should be concurrently mediated by the thermodynamics and growth kinetics, and the selected S/Mo ratio in the CVD process is thus proposed to determine the domain orientations and the edge morphologies.

To probe the electronic properties of monolayer MoS_2 aggregates with and without GBs, back-gated field-effect transistors (FETs) were then fabricated on the samples transferred on 300 nm thick SiO_2/Si substrates, with the schematic structures shown in **Figure 6**a,c. Typical transfer curves were captured on the two kinds of devices with channel length/width of 4/12 µm (Figure 6b,d). Statistically, the average carrier mobilities and on-off ratios for the FET devices based on monolayer MoS_2 without GBs are measured to be ≈44 $cm^2\ V^{-1}s^{-1}$ and $\approx 10^7$, respectively, much higher than that for the ones with the overlapping GBs (≈14 $cm^2\ V^{-1}s^{-1}$ and $\approx 10^6$) (Figure 6e,f). Moreover, both the mobility and on-off ratio of the devices across the seamlessly stitched monolayer MoS_2 edges show a narrow distribution, i.e., 40.1–50.3 $cm^2\ V^{-1}s^{-1}$ and 1.9×10^6–3.4×10^8, respectively. These values are comparable with those achieved on the CVD-derived monolayer triangular domains on sapphire and SiO_2/Si substrates (Table S1, Supporting Information).[26,28,30,35,42–45] In contrast, the FET devices across the overlapping GBs (Figure 6b) exhibit much lower values and relatively discrete characteristics, i.e., 0.1–25.9 $cm^2\ V^{-1}s^{-1}$ and 9.1×10^4–5.4×10^7, respectively. Accordingly, the monolayer MoS_2 merged by two unidirectionally aligned triangular domains presents superior electronic performances than that of disoriented domains with overlapping GBs. Hereby, monolayer MoS_2 single crystal wafers with high crystal quality can serve as perfect channel materials for the fabrication of highly integrated electronic devices.

3. Conclusion

In conclusion, we have realized the high-reproducible, high-efficiency growth of wafer-scale monolayer MoS_2 single crystals

© 2023 Wiley-VCH GmbH

23669608, 2023, 7, Downloaded from https://onlinelibrary.wiley.com/doi/10.1002/smtd.202300165 by Peking University Health, Wiley Online Library on [16/11/2023]. See the Terms and Conditions (https://onlinelibrary.wiley.com/terms-and-conditions) on Wiley Online Library for rules of use; OA articles are governed by the applicable Creative Commons License

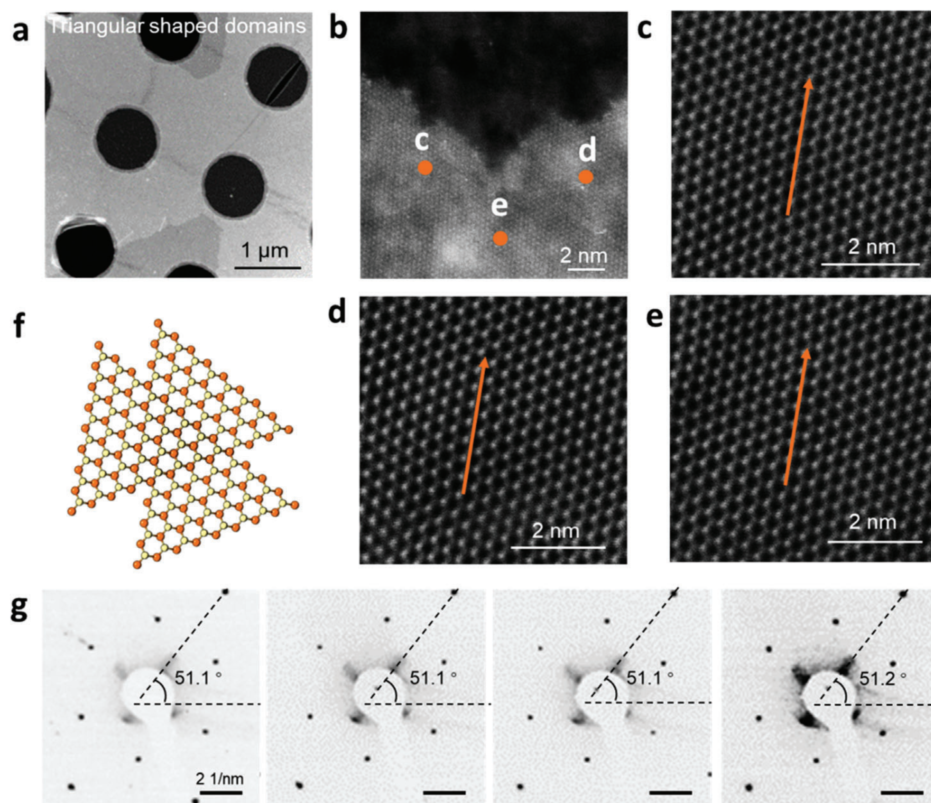

Figure 5. TEM characterizations revealing the seamless stitching of unidirectionally aligned monolayer MoS_2 triangular domains at an atomic scale. a) OM image of the unidirectional aligned monolayer MoS_2 triangular domains transferred on a TEM grid. b) Representative STEM image of the merging area of two adjacent monolayer triangular MoS_2 domains. c–e) Atomic-resolution STEM images recorded at the typical locations marked in (b), involving two stitched domains and the stitching boundary, respectively. f) Schematic illustration of the seamless stitching behavior. g) Randomly selected SAED patterns from the monolayer MoS_2 aggregate merged by unidirectional aligned triangular domains. The angles (with regard to the horizontal direction) marked by the dashed lines are nearly identical (~51.1°, 51.1°, 51.1°, 51.2°), indicating the uniform orientation of the monolayer MoS_2 film.

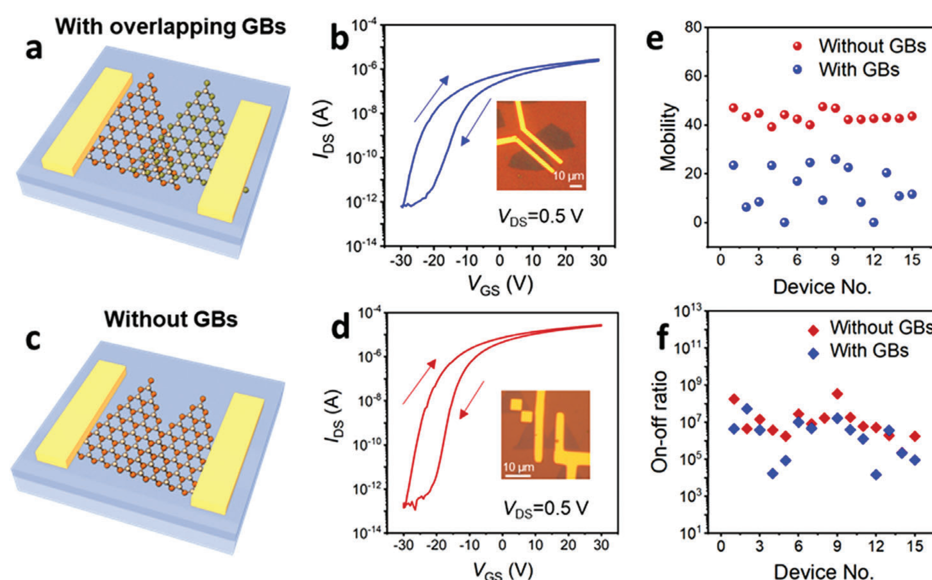

Figure 6. Electronic performances of monolayer MoS_2 aggregates patched by uniformly oriented or disoriented domains featuring with and without GBs, respectively. a,c) Schematic illustration of the devices based on monolayer MoS_2 aggregates composed by two domains with and without GBs, respectively. b,d) Corresponding I_{DS}–V_{GS} curves for the two types monolayer MoS_2 aggregates-based devices (V_{DS} = 0.5 V). Inset: OM images of the monolayer MoS_2-based devices. e,f) Comparison of the carrier mobilities and on/off ratios of the two types FET devices based on monolayer MoS_2 aggregates involved with and without GBs. The FET devices across the boundaries of uniformly oriented MoS_2 domains (without GBs) present higher carrier mobility than that across the GBs evolved from two adjacent disoriented monolayer MoS_2 domains.

© 2023 Wiley-VCH GmbH

on the industrial compatible sapphire substrates, by creatively combining a well-designed "face-to-face" metal precursor releasing route, carbon-cloth-filter based precursor concentration decay strategy, and an adequate optimization of the S/Mo ratio. The size of MoS_2 single crystals can be further scaled up by simply enlarging the furnace sizes, by virtue of the uniform and moderate supply of metal precursors designed in this route. The growth efficiency of the current route is about six times faster than that of traditional upstream metal precursor feeding route. Moreover, we find that the growth kinetics control by selecting a high S/Mo precursor ratio is critical for the unidirectional alignment of monolayer MoS_2 single crystals, which is a significant complement to the existing thermodynamic viewpoints regarding the substrate-step-edge-guiding and the adlayer-substrate-lattice-matching effects. This work hereby provides a multi-aspect synergetic optimization route for the high-reproducible production of wafer-scale 2D single crystals, thus laying foundations for their industrial applications in next-generation highly integrated nanoelectronics.

4. Experimental Section

Epitaxial Growth of 2-inch Wafer-Scale Monolayers MoS_2 Single-Crystals on Sapphire: In prior to the growth of monolayer MoS_2, the as-prepared C-A 1° sapphire substrates (2 inches) were annealed in an oxygen atmosphere at ≈1200 °C for ≈5 h, to form roughly parallel and periodically spaced steps. The epitaxial growth of monolayer MoS_2 single-crystals on sapphire was performed inside a 3-inch diameter quartz tube in a low-pressure CVD system. A 6 × 6 cm^2 Mo foil (≈99.95%, 0.025 nm thick) was folded into a bridge and placed over the sapphire substrate with a distance of ≈1 cm. The sulfur powder (≈99.5%, 10 g) was placed on the upstream region, ≈10 cm away from the sapphire substrate. A 6 × 6 cm^2 carbon cloth was placed on the sapphire substrate to physically prevent the excess deposition of metal-based precursors. Then, the sapphire substrate and Mo foil were heated to ≈950 °C in the protection of Ar (100 sccm) and O_2 (1 sccm) carrier gases within 50 min. After holding the temperature for 10 min, the furnace was cooled down to room temperature naturally. Notably, except for a high S/Mo ratio, a relatively high growth temperature is also conducive to the unidirectional alignment of monolayer MoS_2 domains (Figure S8, Supporting Information).

Characterizations: OM (Nikon ECLIPSE, LV100ND), Raman, PL, and SHG spectroscopy (HORIBA, Lab-RAM HR-800, with an excitation wavelength 532 nm; WITec, Alpha 300R), AFM (Bruker, Dimension Icon), XPS (Kratos Analytical AXIS-Ultra with monochromatic Al Kα X-ray), TEM (JEOL JEM-2100F), and STEM (Nion U-HERMES200, 60 kV, convergence semi-angle: 35 mrad), LEED (Advanced 4-grid LEED/Auger) were used to characterize the single crystallinity and large-area uniformity of the MoS_2 monolayers.

Supporting Information

Supporting Information is available from the Wiley Online Library or from the author.

Acknowledgements

P.Y., F.L., and X.L. contributed equally to this work. The work was supported by the National Key Research and Development Program of China (Nos. 2021YFA1202901, 2018YFA0703700), and the National Natural Science Foundation of China (Nos. 51925201, 51991344, 51991340, 52021006, T2188101, 52202157).

Conflict of Interest

The authors declare no conflict of interest.

Data Availability Statement

Research data are not shared.

Keywords

epitaxial growth, single crystal, transition-metal dichalcogenides, wafer-scale

Received: February 11, 2023
Revised: March 13, 2023
Published online: April 10, 2023

[1] Y. Liu, X. Duan, H. J. Shin, S. Park, Y. Huang, X. Duan, *Nature* **2021**, *591*, 43.
[2] Y. Wang, J. C. Kim, Y. Li, K. Y. Ma, S. Hong, M. Kim, H. S. Shin, H. Y. Jeong, M. Chhowalla, *Nature* **2022**, *610*, 61.
[3] L. Liu, C. Liu, L. Jiang, J. Li, Y. Ding, S. Wang, Y. G. Jiang, Y. bin Sun, J. Wang, S. Chen, D. W. Zhang, P. Zhou, *Nat. Nanotechnol.* **2021**, *16*, 874.
[4] A. Sebastian, R. Pendurthi, T. H. Choudhury, J. M. Redwing, S. Das, *Nat. Commun.* **2021**, *12*, 693.
[5] J. Li, X. Yang, Y. Liu, B. Huang, R. Wu, Z. Zhang, B. Zhao, H. Ma, W. Dang, Z. Wei, K. Wang, Z. Lin, X. Yan, M. Sun, B. Li, X. Pan, J. Luo, G. Zhang, Y. Liu, Y. Huang, X. Duan, X. Duan, *Nature* **2020**, *579*, 368.
[6] X. Xu, Z. Zhang, J. Dong, D. Yi, J. Niu, M. Wu, L. Lin, R. Yin, M. Li, J. Zhou, S. Wang, J. Sun, X. Duan, P. Gao, Y. Jiang, X. Wu, H. Peng, R. S. Ruoff, Z. Liu, D. Yu, E. Wang, F. Ding, K. Liu, *Sci. Bull.* **2017**, *62*, 1074.
[7] B. Deng, Z. Pang, S. Chen, X. Li, C. Meng, J. Li, M. Liu, J. Wu, Y. Qi, W. Dang, H. Yang, Y. Zhang, J. Zhang, N. Kang, H. Xu, Q. Fu, X. Qiu, P. Gao, Y. Wei, Z. Liu, H. Peng, *ACS Nano* **2017**, *11*, 12337.
[8] L. Wang, X. Xu, L. Zhang, R. Qiao, M. Wu, Z. Wang, S. Zhang, J. Liang, Z. Zhang, Z. Zhang, W. Chen, X. Xie, J. Zong, Y. Shan, Y. Guo, M. Willinger, H. Wu, Q. Li, W. Wang, P. Gao, S. Wu, Y. Zhang, Y. Jiang, D. Yu, E. Wang, X. Bai, Z. J. Wang, F. Ding, K. Liu, *Nature* **2019**, *570*, 91.
[9] T. A. Chen, C. P. Chuu, C. C. Tseng, C. K. Wen, H. S. P. Wong, S. Pan, R. Li, T. A. Chao, W. C. Chueh, Y. Zhang, Q. Fu, B. I. Yakobson, W. H. Chang, L. J. Li, *Nature* **2020**, *579*, 219.
[10] S. H. Choi, H. J. Kim, B. Song, Y. I. Kim, G. Han, H. T. T. Nguyen, H. Ko, S. Boandoh, J. H. Choi, C. S. Oh, H. J. Cho, J. W. Jin, Y. S. Won, B. H. Lee, S. J. Yun, B. G. Shin, H. Y. Jeong, Y. M. Kim, Y. K. Han, Y. H. Lee, S. M. Kim, K. K. Kim, *Adv. Mater.* **2021**, *33*, 2006601.
[11] J. Li, S. Wang, Q. Jiang, H. Qian, S. Hu, H. Kang, C. Chen, X. Zhan, A. Yu, S. Zhao, Y. Zhang, Z. Chen, Y. Sui, S. Qiao, G. Yu, S. Peng, Z. Jin, X. Liu, *Small* **2021**, 2100743.
[12] P. Zheng, W. Wei, Z. Liang, B. Qin, J. Tian, J. Wang, R. Qiao, Y. Ren, J. Chen, C. Huang, X. Zhou, G. Zhang, Z. Tang, D. Yu, F. Ding, K. Liu, X. Xu, *Nat. Commun.* **2023**, *14*, 592.
[13] P. Yang, S. Zhang, S. Pan, B. Tang, Y. Liang, X. Zhao, Z. Zhang, J. Shi, Y. Huan, Y. Shi, S. J. Pennycook, Z. Ren, G. Zhang, Q. Chen, X. Zou, Z. Liu, Y. Zhang, *ACS Nano* **2020**, *14*, 5036.
[14] P. Yang, D. Wang, X. Zhao, W. Quan, Q. Jiang, X. Li, B. Tang, J. Hu, L. Zhu, S. Pan, Y. Shi, Y. Huan, F. Cui, S. Qiao, Q. Chen, Z. Liu, X. Zou, Y. Zhang, *Nat. Commun.* **2022**, *13*, 3238.
[15] J. Hu, W. Quan, P. Yang, F. Cui, F. Liu, L. Zhu, S. Pan, Y. Huan, F. Zhou, J. Fu, G. Zhang, P. Gao, Y. Zhang, *ACS Nano* **2022**, *17*, 312.
[16] Z. Q. Xu, Y. Zhang, S. Lin, C. Zheng, Y. L. Zhong, X. Xia, Z. Li, P. J. Sophia, M. S. Fuhrer, Y. B. Cheng, Q. Bao, *ACS Nano* **2015**, *9*, 6178.

© 2023 Wiley-VCH GmbH

23669608, 2023, 7, Downloaded from https://onlinelibrary.wiley.com/doi/10.1002/smtd.202300165 by Peking University Health, Wiley Online Library on [16/11/2023]. See the Terms and Conditions (https://onlinelibrary.wiley.com/terms-and-conditions) on Wiley Online Library for rules of use; OA articles are governed by the applicable Creative Commons License

[17] M. Chubarov, T. H. Choudhury, D. R. Hickey, S. Bachu, T. Zhang, A. Sebastian, A. Bansal, H. Zhu, N. Trainor, S. Das, M. Terrones, N. Alem, J. M. Redwing, *ACS Nano* **2021**, *15*, 2532.
[18] T. Li, W. Guo, L. Ma, W. Li, Z. Yu, Z. Han, S. Gao, L. Liu, D. Fan, Z. Wang, Y. Yang, W. Lin, Z. Luo, X. Chen, N. Dai, X. Tu, D. Pan, Y. Yao, P. Wang, Y. Nie, J. Wang, Y. Shi, X. Wang, *Nat. Nanotechnol.* **2021**, *16*, 1201.
[19] J. Wang, X. Xu, T. Cheng, L. Gu, R. Qiao, Z. Liang, D. Ding, H. Hong, P. Zheng, Z. Zhang, Z. Zhang, S. Zhang, G. Cui, C. Chang, C. Huang, J. Qi, J. Liang, C. Liu, Y. Zuo, G. Xue, X. Fang, J. Tian, M. Wu, Y. Guo, Z. Yao, Q. Jiao, L. Liu, P. Gao, Q. Li, R. Yang, et al., *Nat. Nanotechnol.* **2022**, *17*, 33.
[20] A. Aljarb, Z. Cao, H.-L. Tang, J.-K. Huang, M. Li, W. Hu, L. Cavallo, L.-J. Li, *ACS Nano* **2017**, *11*, 9215.
[21] P. Yang, L. Zhu, F. Zhou, Y. Zhang, *Acc Mater Res* **2022**, *3*, 161.
[22] Q. Ji, Y. Zheng, Y. Zhang, Z. Liu, *Chem. Soc. Rev.* **2015**, *44*, 2587.
[23] M. Chhowalla, H. S. Shin, G. Eda, L. J. Li, K. P. Loh, H. Zhang, *Nat. Chem.* **2013**, *5*, 263.
[24] D. Dumcenco, D. Ovchinnikov, K. Marinov, P. Lazić, M. Gibertini, N. Marzari, O. L. Sanchez, Y.-C. Kung, D. Krasnozhon, M.-W. Chen, S. Bertolazzi, P. Gillet, A. Fontcuberta i Morral, A. Radenovic, A. Kis, *ACS Nano* **2015**, *9*, 4611.
[25] R. Shi, R. Shi, P. He, X. Cai, Z. Zhang, W. Wang, J. Wang, J. Wang, X. Feng, Z. Wu, A. Amini, N. Wang, C. Cheng, *ACS Nano* **2020**, *14*, 7593.
[26] H. Yu, M. Liao, W. Zhao, G. Liu, X. J. Zhou, Z. Wei, X. Xu, K. Liu, Z. Hu, K. Deng, S. Zhou, J. A. Shi, L. Gu, C. Shen, T. Zhang, L. Du, L. Xie, J. Zhu, W. Chen, R. Yang, D. Shi, G. Zhang, *ACS Nano* **2017**, *11*, 12001.
[27] J. Zhu, H. Xu, G. Zou, W. Zhang, R. Chai, J. Choi, J. Wu, H. Liu, G. Shen, H. Fan, *J. Am. Chem. Soc.* **2019**, *141*, 5392.
[28] Q. Wang, N. Li, J. Tang, J. Zhu, Q. Zhang, Q. Jia, Y. Lu, Z. Wei, H. Yu, Y. Zhao, Y. Guo, L. Gu, G. Sun, W. Yang, R. Yang, D. Shi, G. Zhang, *Nano Lett.* **2020**, *20*, 7193.
[29] L. Tang, T. Li, Y. Luo, S. Feng, Z. Cai, H. Zhang, B. Liu, H.-M. Cheng, *ACS Nano* **2020**, *14*, 4646.
[30] P. Yang, X. Zou, Z. Zhang, M. Hong, J. Shi, S. Chen, J. Shu, L. Zhao, S. Jiang, X. Zhou, Y. Huan, C. Xie, P. Gao, Q. Chen, Q. Zhang, Z. Liu, Y. Zhang, *Nat. Commun.* **2018**, *9*, 979.
[31] Q. Ji, M. Kan, Y. Zhang, Y. Guo, D. Ma, J. Shi, Q. Sun, Q. Chen, Y. Zhang, Z. Liu, *Nano Lett.* **2015**, *15*, 198.
[32] L. Liu, T. Li, L. Ma, W. Li, S. Gao, W. Sun, R. Dong, X. Zou, D. Fan, L. Shao, C. Gu, N. Dai, Z. Yu, X. Chen, X. Tu, Y. Nie, P. Wang, J. Wang, Y. Shi, X. Wang, *Nature* **2022**, *605*, 69.
[33] A. Aljarb, J. Fu, C.-C. Hsu, C. Chuu, Y. Wan, M. Hakami, D. R. Naphade, E. Yengel, C. Lee, S. Brems, T. Chen, M.-Y. Li, S. Bae, W. Hsu, Z. Cao, R. Albaridy, S. Lopatin, W. Chang, T. D. Anthopoulos, J. Kim, L. Li, V. Tung, *Nat. Mater.* **2020**, *19*, 1300.
[34] X. Yin, Z. Ye, D. A. Chenet, Y. Ye, K. O'Brien, J. C. Hone, X. Zhang, *Science* **2014**, *344*, 488.
[35] Z. Ma, S. Wang, Q. Deng, Z. Hou, X. Zhou, X. Li, F. Cui, H. Si, T. Zhai, H. Xu, *Small* **2020**, *16*, 202000596.
[36] J. Dong, H. Wang, H. Peng, Z. Liu, K. Zhang, F. Ding, *Chem. Sci.* **2017**, *8*, 2209.
[37] B. C. Bayer, S. Caneva, T. J. Pennycook, J. Kotakoski, C. Mangler, S. Hofmann, J. C. Meyer, *ACS Nano* **2017**, *11*, 4521.
[38] Y. Yu, G. S. Jung, C. Liu, Y. C. Lin, C. M. Rouleau, M. Yoon, G. Eres, G. Duscher, K. Xiao, S. Irle, A. A. Puretzky, D. B. Geohegan, *ACS Nano* **2021**, *15*, 4504.
[39] K. v. Bets, N. Gupta, B. I. Yakobson, *Nano Lett.* **2019**, *19*, 2027.
[40] Y. Nie, C. Liang, P. R. Cha, L. Colombo, R. M. Wallace, K. Cho, *Sci. Rep.* **2017**, *7*, 2977.
[41] J. Xu, D. J. Srolovitz, D. Ho, *ACS Nano* **2021**, *15*, 6839.
[42] A. M. van der Zande, P. Y. Huang, D. A. Chenet, T. C. Berkelbach, Y. You, G. H. Lee, T. F. Heinz, D. R. Reichman, D. A. Muller, J. C. Hone, *Nat. Mater.* **2013**, *12*, 554.
[43] D. Fu, X. Zhao, Y. Y. Zhang, L. Li, H. Xu, A. R. Jang, S. I. Yoon, P. Song, S. M. Poh, T. Ren, Z. Ding, W. Fu, T. J. Shin, H. S. Shin, S. T. Pantelides, W. Zhou, K. P. Loh, *J. Am. Chem. Soc.* **2017**, *139*, 9392.
[44] M. C. Chang, P. H. Ho, M. F. Tseng, F. Y. Lin, C. H. Hou, I. K. Lin, H. Wang, P. P. Huang, C. H. Chiang, Y. C. Yang, I. T. Wang, H. Y. Du, C. Y. Wen, J. J. Shyue, C. W. Chen, K. H. Chen, P. W. Chiu, L. C. Chen, *Nat. Commun.* **2020**, *11*, 3682.
[45] G. H. Han, N. J. Kybert, C. H. Naylor, B. S. Lee, J. Ping, J. H. Park, J. Kang, S. Y. Lee, Y. H. Lee, R. Agarwal, A. T. C. Johnson, *Nat. Commun.* **2015**, *6*, 6128.

© 2023 Wiley-VCH GmbH

23669608, 2023, 7, Downloaded from https://onlinelibrary.wiley.com/doi/10.1002/smtd.202300165 by Peking University Health, Wiley Online Library on [16/11/2023]. See the Terms and Conditions (https://onlinelibrary.wiley.com/terms-and-conditions) on Wiley Online Library for rules of use; OA articles are governed by the applicable Creative Commons License